

# Engineering High- $k$ /SiGe Interface with ALD Oxide for Selective $\text{GeO}_x$ Reduction

Mahmut S. Kavrik,<sup>†</sup> Peter Ercius,<sup>§</sup> Joanna Cheung,<sup>†</sup> Kechao Tang,<sup>||</sup> Qingxiao Wang,<sup>⊥</sup> Bernd Fruhberger,<sup>‡</sup> Moon Kim,<sup>⊥</sup> Yuan Taur,<sup>†</sup> Paul C. McIntyre,<sup>||</sup> and Andrew C. Kummel<sup>\*,†,||</sup>

<sup>†</sup>Materials Science and Engineering and <sup>‡</sup>California Institute for Telecommunications and Information Technology, University of California San Diego, La Jolla, California 92093, United States

<sup>§</sup>National Center for Electron Microscopy, Molecular Foundry, Lawrence Berkeley National Laboratory, Berkeley, California 94720, United States

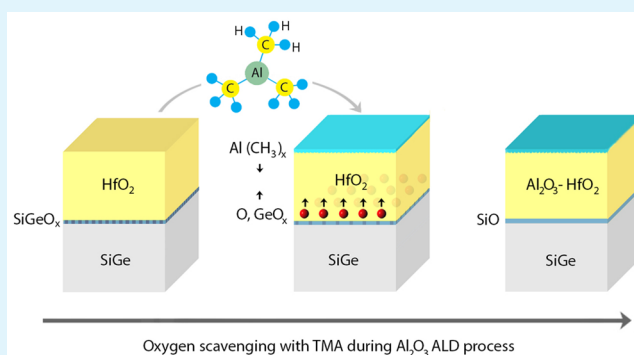
<sup>||</sup>Materials Science and Engineering, Stanford University, Stanford, California 94305, United States

<sup>⊥</sup>Material Science and Engineering, University of Texas, Dallas, Texas 75080-3021, United States

## S Supporting Information

**ABSTRACT:** Suppression of electronic defects induced by  $\text{GeO}_x$  at the high- $k$  gate oxide/SiGe interface is critical for implementation of high-mobility SiGe channels in complementary metal–oxide–semiconductor (CMOS) technology. Theoretical and experimental studies have shown that a low defect density interface can be formed with an  $\text{SiO}_x$ -rich interlayer on SiGe. Experimental studies in the literature indicate a better interface formation with  $\text{Al}_2\text{O}_3$  in contrast to  $\text{HfO}_2$  on SiGe; however, the mechanism behind this is not well understood. In this study, the mechanism of forming a low defect density interface between  $\text{Al}_2\text{O}_3$ /SiGe is investigated using atomic layer deposited (ALD)  $\text{Al}_2\text{O}_3$  insertion into or on top of ALD  $\text{HfO}_2$  gate oxides. To elucidate the mechanism, correlations are made between the defect density determined by impedance measurements and the chemical and physical structures of the interface determined by high-resolution scanning transmission electron microscopy and electron energy loss spectroscopy. The compositional analysis reveals an  $\text{SiO}_x$  rich interlayer for both  $\text{Al}_2\text{O}_3$ /SiGe and  $\text{HfO}_2$ /SiGe interfaces with the insertion of  $\text{Al}_2\text{O}_3$  into or on top of the  $\text{HfO}_2$  oxide. The data is consistent with the  $\text{Al}_2\text{O}_3$  insertion inducing decomposition of the  $\text{GeO}_x$  from the interface to form an electrically passive,  $\text{SiO}_x$  rich interface on SiGe. This mechanism shows that nanolaminate gate oxide chemistry cannot be interpreted as resulting from a simple layer-by-layer ideal ALD process, because the precursor or its reaction products can diffuse through the oxide during growth and react at the semiconductor interface. This result shows that in scaled CMOS, remote oxide ALD (oxide ALD on top of the gate oxide) can be used to suppress electronic defects at gate oxide semiconductor interfaces by oxygen scavenging.

**KEYWORDS:** SiGe CMOS, low-power electronics, high-mobility transistor, high- $k$  dielectrics,  $\text{Al}_2\text{O}_3$ ,  $\text{HfO}_2$  interface trap charge, atomic layer deposition



## INTRODUCTION

SiGe alloys are employed as stressor layers in mainstream complementary metal–oxide–semiconductor (CMOS) transistors and are being investigated as p-type field effect transistor (p-FET) channels due to their high mobility<sup>1</sup> and ease of integration into CMOS.<sup>2</sup> Thermally stable  $\text{HfO}_2$  gate oxides with high dielectric constants reduce CMOS device power consumption.<sup>3,4</sup> SiGe p-FETs with high- $k$  gate dielectrics, which have low defect interfaces, can provide better electrostatic control of the channel and higher drive current for low gate bias voltage. Conversely, a high density of interface defects between the high- $k$  gate oxide and the SiGe channel degrades the device performance metrics, such as subthreshold slope, and reduces the on/off current ratio.<sup>5</sup> The

main challenge for implementing SiGe FETs is the binary atom termination (Si–Ge) of the surface which results in the formation of  $\text{SiGeO}_x$  mixed oxides and dangling bonds on both Si and Ge atoms.<sup>6–8</sup>  $\text{GeO}_x$  and associated dangling bonds are the main sources of defects producing interface-trapped charge ( $D_{it}$ ), whereas  $\text{SiO}_x$  is a stable oxide that forms a nearly defect-free interface according to theoretical calculations.<sup>9</sup>

Previously, several techniques, such as nitride and sulfur passivation on  $\text{Si}_{0.7}\text{Ge}_{0.3}(001)$ , were studied with  $\text{Al}_2\text{O}_3$  gate oxides, and a reduction in the interface defect density via

Received: December 25, 2018

Accepted: April 2, 2019

Published: April 2, 2019

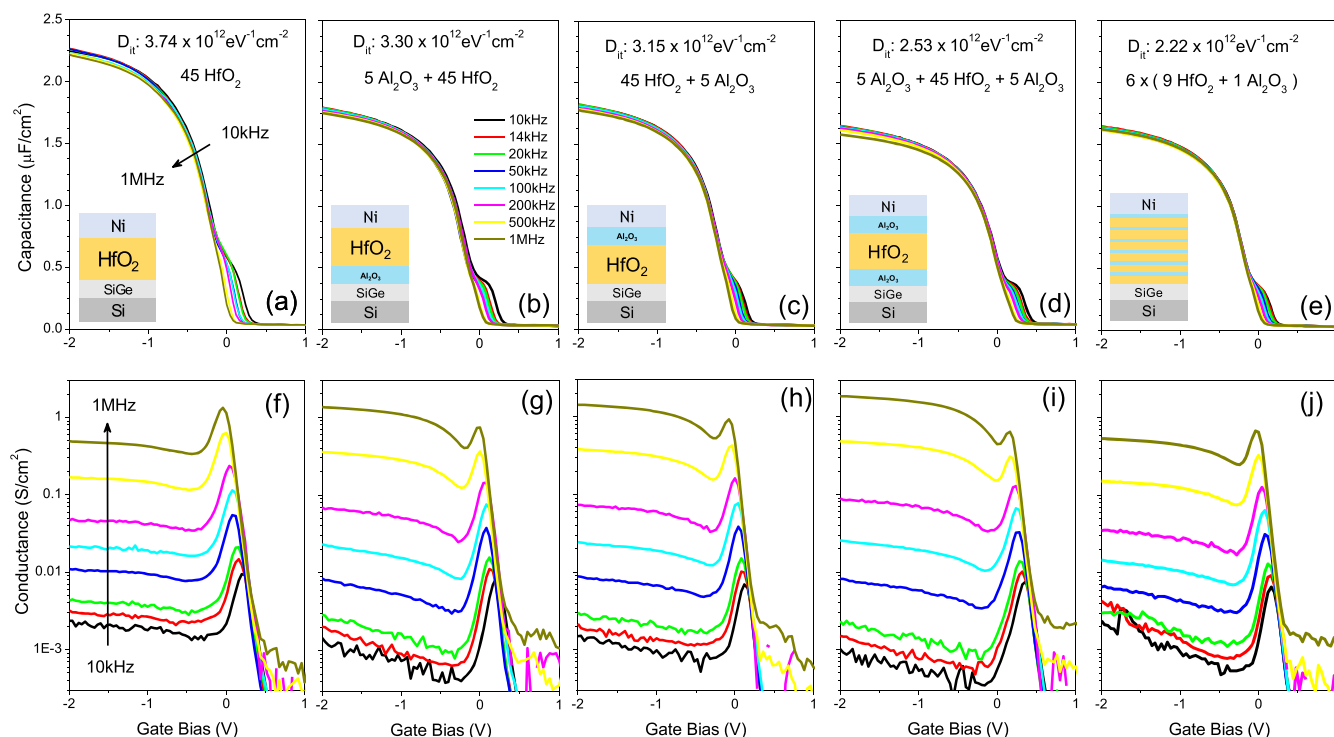


**Figure 1.** C–V and G–V graphs of multilayer MOSCAP devices (a–j). Inset drawings indicate a device structure for the given graph. The inset  $D_{it}$  values indicate the peak interface defect density value in the band gap obtained with a full interface state model (FISM). The energy distribution of the defects density and the energy of the peak  $D_{it}$  values in the band gap are shown in Figure 4. A control device with HfO<sub>2</sub> gate oxide shows the highest interface defect density of  $3.74 \times 10^{12} \text{ eV}^{-1} \text{ cm}^{-2}$ . Al<sub>2</sub>O<sub>3</sub> insertion into HfO<sub>2</sub> reduces  $D_{it}$  gradually by going from the HfO<sub>2</sub>–Al<sub>2</sub>O<sub>3</sub> bilayer into the Al<sub>2</sub>O<sub>3</sub>–HfO<sub>2</sub>–Al<sub>2</sub>O<sub>3</sub> trilayer and finally nanolaminate gate oxides to  $D_{it} = 2.22 \times 10^{12} \text{ eV}^{-1} \text{ cm}^{-2}$ . Al<sub>2</sub>O<sub>3</sub> insertion reduces  $D_{it}$  regardless of its position shows a significant impact of oxygen scavenging.

suppression of GeO<sub>x</sub> formation was reported.<sup>10,11</sup> However, similar low defect density interfaces could not be established with HfO<sub>2</sub> gate oxide. This is because oxygen containing species, such as excess H<sub>2</sub>O, OH, and/or O, can diffuse through HfO<sub>2</sub> during atomic layer deposition (ALD), forming GeO<sub>x</sub> defects on the SiGe surface; in addition, the nature of HfO<sub>2</sub> allows diffusion of Ge and GeO<sub>x</sub> to the top surface of the oxide and TMA induced GeO<sub>2</sub> decomposition.<sup>8,11–13</sup> Recently, HfO<sub>2</sub>/SiGe interfaces formed with Al<sub>2</sub>O<sub>3</sub>–HfO<sub>2</sub> nanolaminate (NL) gate dielectric stacks were found to have a low interface state density, and it was hypothesized that the mechanism was reduction of GeO<sub>x</sub> out-diffusion during ALD.<sup>14</sup> Theoretical density functional theory (DFT) models of the amorphous HfO<sub>2</sub>/Si<sub>0.5</sub>Ge<sub>0.5</sub>(001) interface have shown that low defect interfaces may be formed even before hydrogen passivation with short anneals (<10 ps) when the interface is comprised solely of silicon monoxide (SiO).<sup>15</sup> Experimental studies have shown a  $10\times D_{it}$  reduction at the Al<sub>2</sub>O<sub>3</sub>/SiGe and HfO<sub>2</sub>/SiGe interfaces via selective oxygen scavenging by using an oxygen scavenging, metallic Al gate;<sup>16</sup> the selectivity is due to the difference in the formation enthalpy of GeO<sub>x</sub> compared to SiO<sub>x</sub> facilitating transfer of oxygen from GeO<sub>x</sub> to Al.<sup>6,16</sup> However, this process induced thicker gate oxides and reduced the maximum capacitance density ( $C_{max}$ ) resulting from Al oxidation on top of ALD-grown gate oxide.

In the present study, the formation of low interface defect density HfO<sub>2</sub>/SiGe gate stacks using inorganic and organo-metallic -based ALD Al<sub>2</sub>O<sub>3</sub> insertion in bilayers and nanolaminates of Al<sub>2</sub>O<sub>3</sub> and HfO<sub>2</sub> was investigated with scanning transmission electron microscopy (STEM)–electron energy loss spectroscopy (EELS) analysis. It is found that the insertion

of the highly oxygen reactive trimethyl aluminum (TMA) ALD precursor for Al<sub>2</sub>O<sub>3</sub> in HfO<sub>2</sub> containing gate stacks reduces defects consistent with the remote selective oxygen scavenging from the interface. This new selective oxygen scavenging technique is most effective when Al<sub>2</sub>O<sub>3</sub> layers are uniformly distributed across the HfO<sub>2</sub> in a nanolaminate (NL) structure, but it also is effective when the Al<sub>2</sub>O<sub>3</sub> ALD deposition occurs on top of the HfO<sub>2</sub>. In Al<sub>2</sub>O<sub>3</sub> ALD, during each TMA half cycle, the TMA is dosed in excess; therefore, after the surface hydroxyl groups are eliminated, the TMA is available to reduce additional species either by diffusion through HfO<sub>2</sub> or remotely at the growth surface. This is consistent with GeO<sub>x</sub> out-diffusing to the top of HfO<sub>2</sub> gate oxides<sup>11,13,17</sup> and the TMA remotely reducing the GeO<sub>x</sub> during each half cycle.<sup>13</sup> It is found that using the Al<sub>2</sub>O<sub>3</sub> ALD prior to HfO<sub>2</sub> deposition is not as effective as using the Al<sub>2</sub>O<sub>3</sub> ALD in the nanolaminate, consistent with the suggestion that gettering is most effective after deposition of sufficient oxide to act as an H<sub>2</sub>O barrier to reduce the additional formation of GeO<sub>x</sub> during water-based ALD. This hypothesis of the gate oxide acting as a H<sub>2</sub>O barrier and TMA being a GeO<sub>x</sub> reducing agent was supported by experiments with ALD of purely Al<sub>2</sub>O<sub>3</sub> gates, because Al<sub>2</sub>O<sub>3</sub> is a better diffusion barrier than HfO<sub>2</sub>.<sup>13</sup> Oxygen vacancies in HfO<sub>2</sub> are well documented, and the prevention of Ge out-diffusion with Al<sub>2</sub>O<sub>3</sub> incorporation into gate oxide is shown.<sup>11,13</sup> Once the Al<sub>2</sub>O<sub>3</sub> gate oxide reaches a critical thickness, an additional 25% increase in oxide thickness results in a 4× reduction in  $D_{it}$  and nearly a complete elimination of the SiGeO<sub>x</sub> interfacial layer (IL). For HfO<sub>2</sub>, the selective scavenging process benefits from the difference in the formation enthalpy of SiO<sub>x</sub> in comparison to GeO<sub>x</sub> and

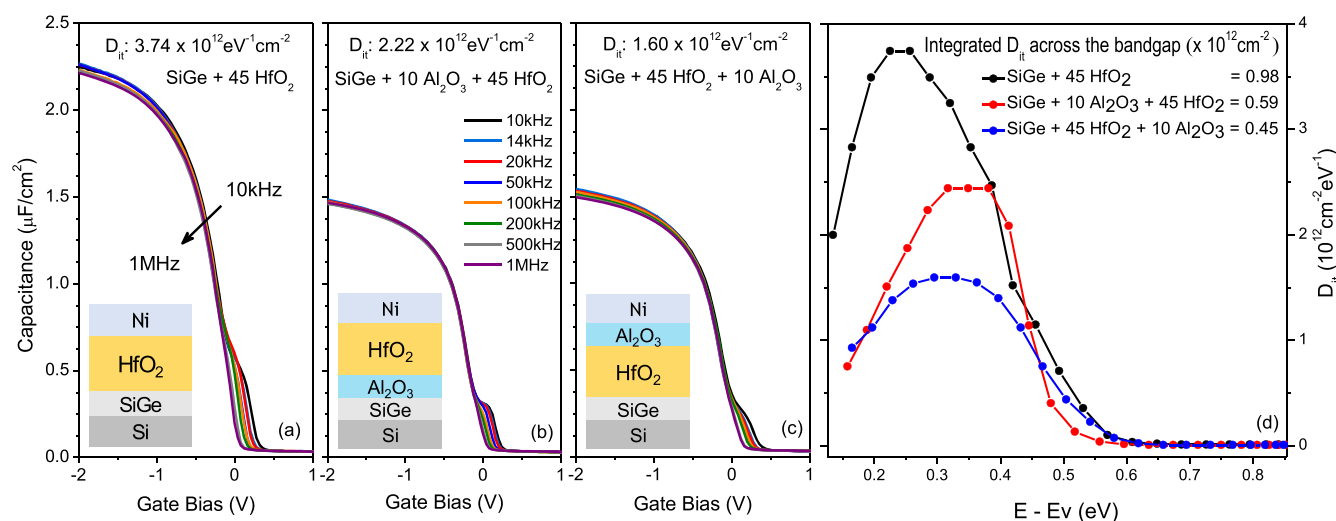


**Figure 2.** C–V graphs and interface defect density distributions across the band gap for MOSCAP devices calculated with the full interface state model. Inset drawings indicate the device structure for the given graph. The inset  $D_{it}$  values indicate the peak interface defect density value in the band gap obtained with a full interface state model. (a) The control device with  $\text{HfO}_2$  gate oxide shows the highest interface defect density of  $D_{it}$  (peak) =  $3.74 \times 10^{12} \text{ eV}^{-1} \text{ cm}^{-2}$ . (b) Interface defects at SiGe oxide interface decrease by the insertion of 10 cycles of  $\text{Al}_2\text{O}_3$  monolayers before  $\text{HfO}_2$   $D_{it}$  (peak) =  $2.22 \times 10^{12} \text{ eV}^{-1} \text{ cm}^{-2}$  and (c) after  $\text{HfO}_2$   $D_{it}$  (peak) =  $1.6 \times 10^{12} \text{ eV}^{-1} \text{ cm}^{-2}$  gate oxide. (d) Comparison of the defect density at the SiGe oxide interface across the band gap shows a decrease in the peak and integrated  $D_{it}$  (inset) by the insertion of  $\text{Al}_2\text{O}_3$  layers.

**Table 1.** Comparison of  $D_{it}$  Values Obtained with Conductance and Full Interface State Model

MOSCAP devices in SiGe/.../Ni	$C_{ox}$ ( $\mu\text{F cm}^{-2}$ )	$V_{fb}$ (V)	$D_{it}$ CM ( $\text{cm}^{-2} \text{ eV}^{-1}$ )	$D_{it}$ FISM ( $\text{cm}^{-2} \text{ eV}^{-1}$ )	standard errors of the mean	standard errors (%)
45 $\text{HfO}_2$	2.5	−0.02	3.57	3.74	0.266	7.1
$\text{SAI}_2\text{O}_3/45 \text{ HfO}_2$	1.96	−0.03	2.43	3.30	0.074	2.2
45 $\text{HfO}_2/\text{SAI}_2\text{O}_3$	2.02	−0.01	2.35	3.15	0.10	3.1
$\text{SAI}_2\text{O}_3/45 \text{ HfO}_2/\text{SAI}_2\text{O}_3$	1.74	0.12	2.18	2.53	0.124	4.9
$6 \times (9\text{HfO}_2 + 1\text{Al}_2\text{O}_3)$	1.8	−0.05	2.02	2.22	0.05	2.2

reduces the interface-trapped charge density by forming Si rich  $\text{SiO}_x$  at the interface, consistent with the predictions of the DFT models.<sup>15</sup> This is also consistent with the known ability of TMA to reduce low enthalpy of formation oxides on substrates at the start of ALD, a process known as ALD cleanup.<sup>18,19</sup>

## METHODS

Metal–oxide–semiconductor (MOS) capacitor (MOSCAP) devices were fabricated with  $\text{HfO}_2$  and  $\text{Al}_2\text{O}_3$  oxides onto  $\text{Si}_{0.7}\text{Ge}_{0.3}$ (100) epitaxially grown on p-type Si(100) (Applied Materials). Samples were degreased by sonication in methanol for 1 min followed by 10 s rinses in acetone, isopropyl alcohol, and deionized (DI)  $\text{H}_2\text{O}$ . Native oxides were removed by cycling 2.5 times through 1 min 2% hydrofluoric acid (HF) solution and 1 min DI  $\text{H}_2\text{O}$ , ending with 2% HF. The samples were dried in  $\text{N}_2$ , passivated in an ammonium sulfide solution (25%  $(\text{NH}_4)_2\text{S}$ ) for 15 min, rinsed with water for 30 s, and dried with  $\text{N}_2$ . Subsequently, samples were transferred to the atomic layer deposition (ALD) chamber, and oxide structures were grown by using a Beneq TFS200 cross flow reactor at 275 °C using tetrakis dimethyl amino hafnium (TDMAH),  $\text{HfCl}_4$ , and TMA metal precursors and water as an oxidant. Each  $\text{HfO}_2$  cycle consisted of 1 s of a TDMAH or  $\text{HfCl}_4$  pulse and a 500 ms of  $\text{H}_2\text{O}$  pulse, each  $\text{Al}_2\text{O}_3$  cycle consisted of a 1 s TMA pulse and a 500 ms  $\text{H}_2\text{O}$  pulse. Ar was used as a carrier gas for all processes, and 6 s purges were employed between each pulse. A set of samples were fabricated in bilayer, trilayer, and nanolaminate (NL) structures formed by  $\text{Al}_2\text{O}_3$  and  $\text{HfO}_2$  in a gate stack for MOSCAPs, as shown in Figure S1 and the insets of Figure 1. Nickel gates (50 nm thick, 150  $\mu\text{m}$  diameter) were deposited with a shadow mask onto the oxide surface using a Denton 502A thermal evaporator in vacuum  $<2 \times 10^{-6}$ . Al back contacts were deposited by sputtering after native oxide removal with Ar plasma at

100 W, 5 mTorr in a Denton Discovery 635 sputtering system. Samples were annealed using an optimized recipe for 30 min total (10 min at 300 °C, 10 min at 330 °C, and 10 min at 350 °C) in forming gas (5%  $\text{H}_2$ , 95%  $\text{N}_2$ ) in a Ulvac MILA-3000 Minilamp annealer at 3 slpm at 1 atm. MOSCAP characterization at 300 K was performed with Keysight B1500. Multifrequency capacitance–voltage (C–V) and conductance–voltage (G–V) measurements were obtained from 2 kHz to 1 MHz with 30 mV alternating current signal superimposed on a direct current gate bias varied from 2 to −2 V. For the structural and compositional analyses, transmission electron microscopy (TEM) specimens ( $<50 \text{ nm}$ ) were prepared from MOSCAP devices using a FEI-Scios Ga focus ion beam. STEM/TEM analyses on high-k/SiGe gate stacks were carried out with FEI Titan 80–300, FEI Metrios, and JEOL ARM 200CF. STEM high-angle annular dark field (HAADF) and bright field (BF) along with TEM images were obtained. Compositional analysis was performed with electron energy loss spectroscopy (EELS) both at 80 and 200 keV with a JEOL ARM 200CF equipped with a Gatan Quantum EELS spectrometer.

## RESULTS AND DISCUSSION

Electrical characterizations of the MOSCAP devices with various gate oxide structures after forming gas annealing (FGA) are shown in Figure 1. The C–V analyses for 45 cycles ( $\sim 4.5 \text{ nm}$ ) of  $\text{HfO}_2$  control sample with a  $C_{\text{max}}$  of  $2.5 \mu\text{F cm}^{-2}$  and corresponding G–V characterization are presented in Figure 1a,f; a peak defect density of ( $D_{it}$ )  $3.74 \times 10^{12} \text{ eV}^{-1} \text{ cm}^{-2}$  (see Figure 2) is obtained. The full interface state model<sup>20,21</sup> is used to calculate the energy distribution of the  $D_{it}$  by fitting multifrequency C–V and G–V curves for each bias point from inversion (2 V) to accumulation (−1 V). The result peak  $D_{it}$  values from the full interface state model are



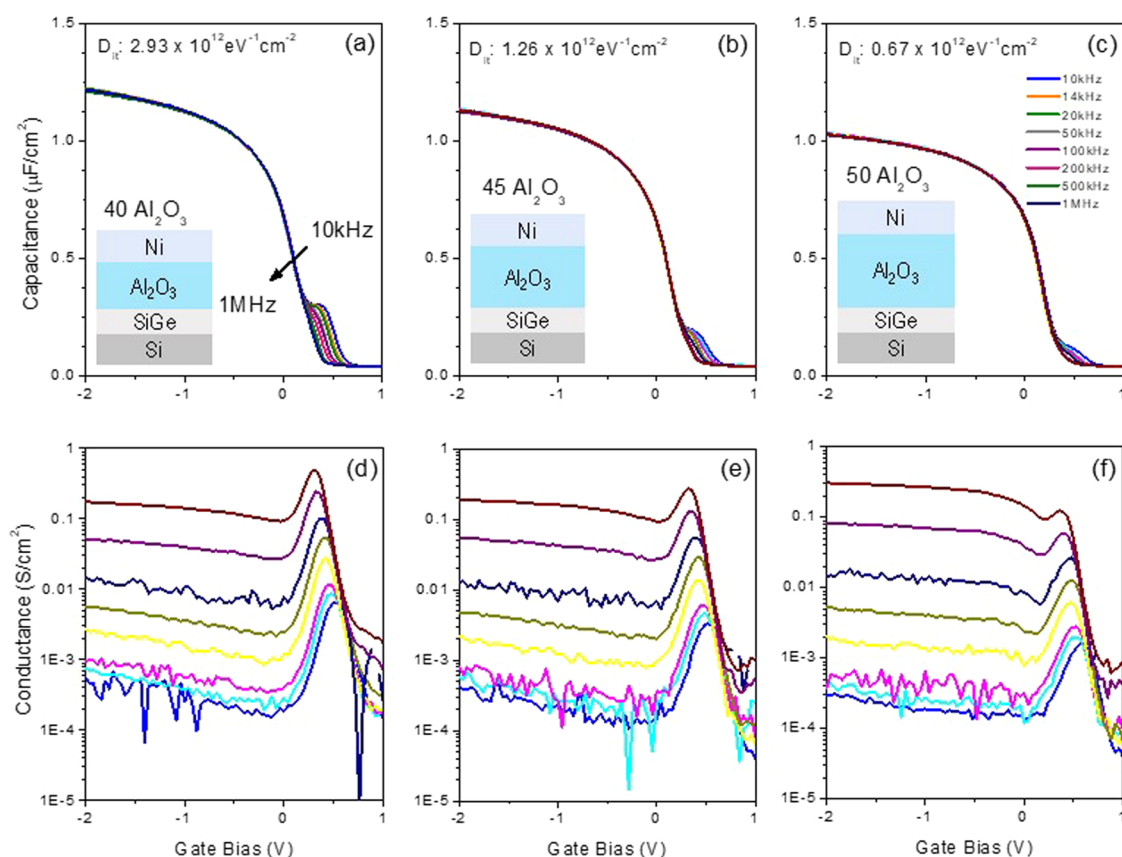


**Figure 3.** C–V and G–V graphs of single-oxide MOSCAP devices (a–f). Inset drawings indicate the device structure for the given graph. The inset  $D_{it}$  values indicate the peak interface defect density value in the band gap obtained with the full interface state model. Control device with 40 cycles of  $\text{Al}_2\text{O}_3$  gate oxide shows the highest interface defect density of  $2.93 \times 10^{12} \text{ eV}^{-1} \text{ cm}^{-2}$ . The small increase of  $\text{Al}_2\text{O}_3$  thickness reduces  $D_{it}$  by  $>4\times$ ; the lowest interface defect density of  $0.67 \times 10^{12} \text{ eV}^{-1} \text{ cm}^{-2}$  is obtained with 50 cycles of  $\text{Al}_2\text{O}_3$ .

compared with the  $D_{it}$  values from the conductance method (CM)<sup>22</sup> and shown to be in agreement, as documented in Table 1. Figure 1b,c shows the C–V for five cycles of  $\text{Al}_2\text{O}_3$  insertion below and above 45 cycles of  $\text{HfO}_2$ . As expected,  $\text{Al}_2\text{O}_3$  insertion decreases  $C_{\text{max}}$  in both cases due to an increase in total oxide thickness and the lower dielectric constant of  $\text{Al}_2\text{O}_3$  in comparison to  $\text{HfO}_2$ . However, the magnitude of the dispersive, depletion capacitance  $D_{it}$  feature also decreases, as shown in Figure 1b,c.  $\text{Al}_2\text{O}_3$  insertion below or above  $\text{HfO}_2$  has a nearly identical effect on an interface defect density corresponding to peak  $D_{it}$  values of  $3.30 \times 10^{12} \text{ eV}^{-1} \text{ cm}^{-2}$  and  $3.15 \times 10^{12} \text{ eV}^{-1} \text{ cm}^{-2}$ . Note that full  $D_{it}$  distributions as a function of the thickness are shown below confirming the trends. Because interface trap response involves defects at the semiconductor oxide interface, a change in  $D_{it}$  resulting from the addition of five ALD cycles of  $\text{Al}_2\text{O}_3$  on top of a 4.5 nm thick  $\text{HfO}_2$  layer is unexpected. Moreover, as shown in Figure 1d,  $\text{Al}_2\text{O}_3$  insertion both above and below  $\text{HfO}_2$  in an  $\text{Al}_2\text{O}_3/\text{HfO}_2/\text{Al}_2\text{O}_3$  trilayer structure further decreases the interface-trapped charge density by 10% to  $2.53 \times 10^{12} \text{ eV}^{-1} \text{ cm}^{-2}$ . Furthermore, as shown in Figure 1e, when  $\text{Al}_2\text{O}_3$  layers dispersed across the  $\text{HfO}_2$  in the nanolaminate structure (NL), the  $D_{it}$  decreases further down to  $2.22 \times 10^{12} \text{ eV}^{-1} \text{ cm}^{-2}$ , 12% lower than the trilayer with a small increase in  $C_{\text{max}}$ . The  $C_{\text{max}}$  reduction due to an increase in total oxide thickness is expected, but  $D_{it}$  reduction with more  $\text{Al}_2\text{O}_3$  incorporation remote from the interface is not.

To better document the effects of bottom versus top  $\text{Al}_2\text{O}_3$ , samples were grown with 10 cycles of  $\text{Al}_2\text{O}_3$  inserted either below the  $\text{HfO}_2$  or above the  $\text{HfO}_2$ . This caused very large decreases in  $D_{it}$ , as shown in Figure 2. Again, the deposition of  $\text{Al}_2\text{O}_3$  on top of the  $\text{HfO}_2$  induced a 57% decrease in the peak  $D_{it}$  as well as a 54% decrease in the integrated  $D_{it}$ , whereas the  $\text{Al}_2\text{O}_3$  inserted below the  $\text{HfO}_2$  only induced a 40% decrease in the peak  $D_{it}$  as well as a 40% decrease in the integrated  $D_{it}$ . The integrated  $D_{it}$  is obtained by the summation of the defect densities across the band gap in Figure 4; this is equivalent to the integration of the areas under the  $D_{it}$  curves; these integrated  $D_{it}$  are a measure of the total defects induced in the band gaps. Curves provide total defects induced in the band gap.

For the five cycles of  $\text{Al}_2\text{O}_3$  insertion, although absolute defect density quantification is challenging, small decreases in the magnitude of the interface trap-related depletion capacitance feature while maintaining an essentially constant  $C_{\text{max}}$  suggest a lower defect density at the interface oxide/semiconductor interface for the nanolaminate structure compared to the trilayer sample or the bilayer samples. For each processing condition, 5–10 devices were studied. The two to three devices with the most consistent C–V were chosen for further analysis. Therefore, although absolute  $D_{it}$  calculations are accurate only within 30%; even 10% changes in  $D_{it}$  decay with  $\text{Al}_2\text{O}_3$  insertion are reliable as confirmed via the fabrication of multiple sample sets, as shown in Figure S8. The  $D_{it}$  standard errors of the mean (in  $\text{cm}^{-2} \text{ eV}^{-1}$  and percentage)

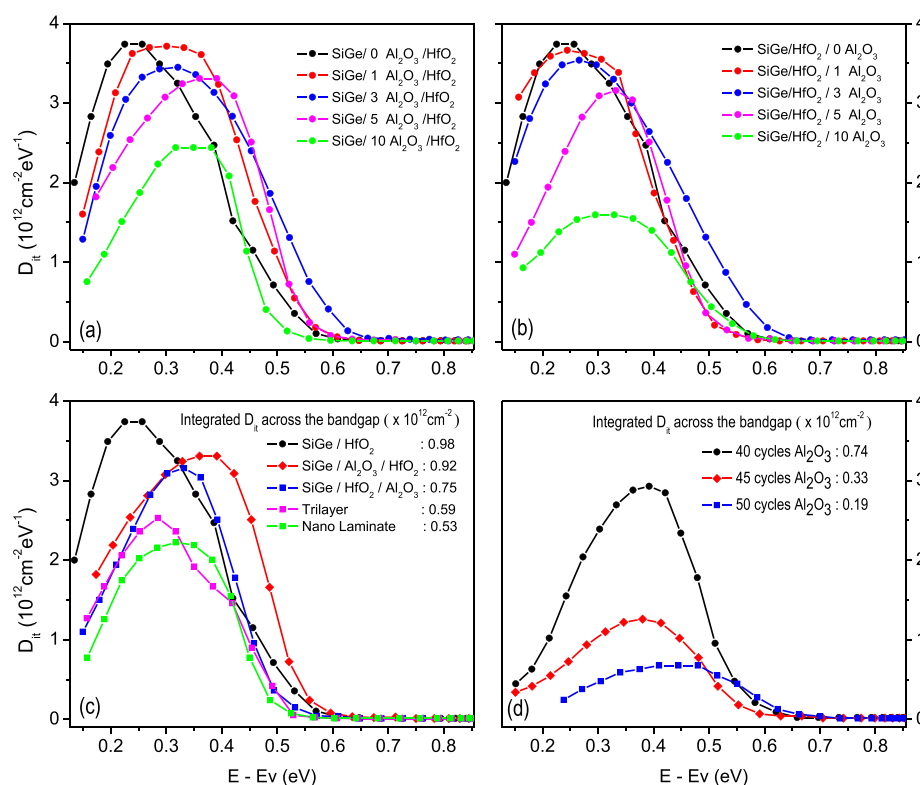


**Figure 4.** Interface defect density distributions across the band gap for MOSCAP devices calculated with the full interface state model. Interface defects at SiGe–oxide interface decrease by the insertion of Al<sub>2</sub>O<sub>3</sub> layers before HfO<sub>2</sub> (a) and after HfO<sub>2</sub> (b) gate oxide. (c) Comparison of the interface defects variation at the SiGe–oxide interface by the insertion of Al<sub>2</sub>O<sub>3</sub> layers into the HfO<sub>2</sub> gate oxide. (d) Interface defect density decreases by an increase in the Al<sub>2</sub>O<sub>3</sub> thickness. For 50 cycles of Al<sub>2</sub>O<sub>3</sub>, peak  $D_{it}$  reduces to  $6 \times 10^{11} \text{ eV}^{-1} \text{ cm}^{-2}$  and integrated defects across the band gap are as low as  $0.19 \times 10^{11} \text{ eV}^{-1} \text{ cm}^{-2}$ .

for samples were calculated, as shown in Table 1. The typical standard error is 3.9%, and changes in  $D_{it}$  of 10% are significant in this comparison. The  $D_{it}$  standard error analysis has shown that changes in  $D_{it}$  of 10% can reliably be determined. Error bars are not given for each data point since the absolute  $D_{it}$  is less precisely determined in part because the uncertainty in  $C_{ox}$  is about 10% which can translate into 10–20% uncertainty in absolute  $D_{it}$ .<sup>22</sup> Additional details for standard error analysis are shown in Table 1. As shown in Table 1, there is no significant change for  $V_{fb}$  as a function of processing conditions. In addition, there is a very little dependence of  $V_{fb}$  on frequency; however, when there is frequency dependence, the highest frequency C–V is employed to access  $V_{fb}$  since it is least affected by traps.

To investigate the mechanism of  $D_{it}$  reduction due to the insertion of Al<sub>2</sub>O<sub>3</sub> ALD layers, MOSCAP devices with only Al<sub>2</sub>O<sub>3</sub> gate oxides of varying thickness were prepared, as shown in Figure 3. As expected, C–V and G–V measurements from Al<sub>2</sub>O<sub>3</sub> devices after FGA as a function of deposition cycles or oxide thickness show a decrease in  $C_{max}$  from  $1.3 \mu\text{F cm}^{-2}$  to  $1.0 \mu\text{F cm}^{-2}$  by increasing the oxide thickness. The depletion capacitance  $D_{it}$  feature also decreases in amplitude. Once the ALD-grown oxide thickness increases above a critical value, there is a superlinear decrease in  $D_{it}$ . For an increase of 25% in the number ALD cycles (40–50 cycles), the  $D_{it}$  decreases by  $>4\times$  from  $2.93 \times 10^{12}$  to  $0.67 \times 10^{12} \text{ eV}^{-1} \text{ cm}^{-2}$ . The lower  $D_{it}$  from increasing the number of ALD cycle from 40 to 50 is not the result of a sudden increase in the oxide thickness due to an ALD onset delay. The  $C_{max}$  for 50 cycles is just 25% lower than for 40 cycles consistent with nearly linear growth. Because the

$D_{it}$  originates from defects at the interface with the semiconductor,  $D_{it}$  reduction by growing additional Al<sub>2</sub>O<sub>3</sub> layers is consistent with the chemical modification of the interface by exposure to the TMA-based ALD environment. The C–V curves obtained from MOS capacitors containing Al<sub>2</sub>O<sub>3</sub> before FGA shown in Figure S4 exhibit a similar trend. It is noted that for Si interfaces, Al<sub>2</sub>O<sub>3</sub> ALD is reported to reduce defects by a post deposition hydrogen passivation mechanism. However, for SiGe, the most important dangling bonds are on Ge which are not readily passivated by hydrogen as shown by the lowest  $D_{it}$  devices being ones which eliminate interfacial GeO<sub>x</sub> using a gettering gate. This is also consistent with previous reports of extremely low  $D_{it}$  for HfO<sub>2</sub>/SiGe by the deposition of Al gettering metal on top of HfO<sub>2</sub> in which the FGA was performed after Al deposition.<sup>16</sup>

The suppression of the interface defects with the Al<sub>2</sub>O<sub>3</sub> insertion into gate oxide influences is not limited to a single energy but is distributed across the band gap as shown in the  $D_{it}$  energy distributions extracted from measured C–V and conductance–voltage (G–V) data using the full interface state model,<sup>20</sup> as shown in Figure 4. Note that interface defect distribution across the band gap for all of the devices in this work is summarized in Figure 4 side by side for a better comparison. In addition, the insertion of 1, 3, 5, and 10 monolayers of Al<sub>2</sub>O<sub>3</sub> below HfO<sub>2</sub> (Figure S2) and on top of HfO<sub>2</sub> (Figure S3) was studied via C–V and G–V and indicates similar trends. Trapped charge energy distributions of the corresponding capacitors shown in Figure 4a,b are consistent with Figure 1 and show a decrease of  $D_{it}$  with the incorporation of Al<sub>2</sub>O<sub>3</sub> ALD layers but below and above

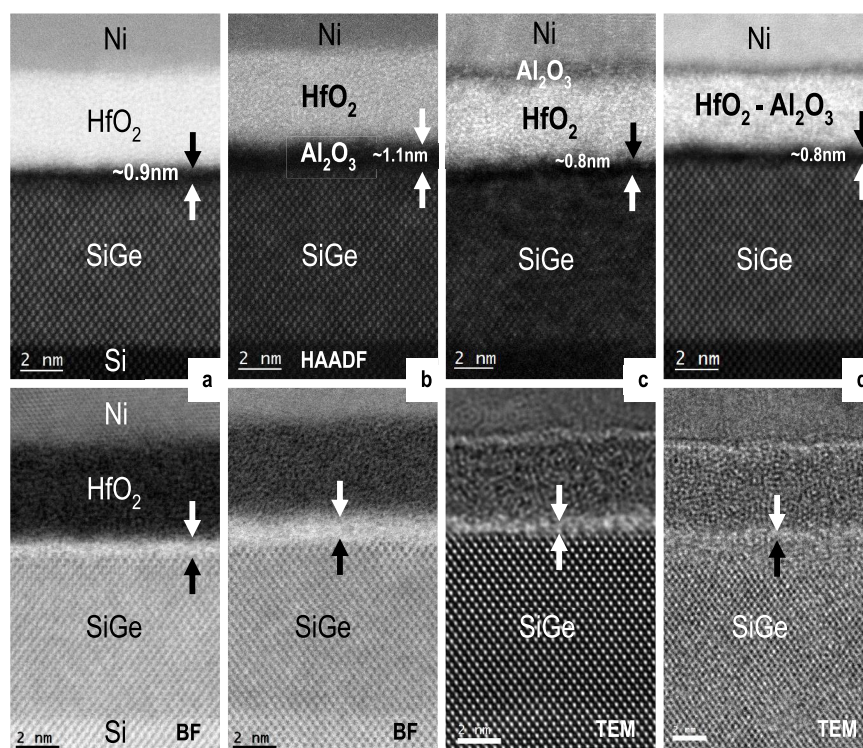


**Figure 5.** STEM high-angle annular dark-field (HAADF), BF (bright field) images of (a) control  $\text{HfO}_2$ , (b)  $\text{HfO}_2/\text{Al}_2\text{O}_3/\text{SiGe}$  bilayer, (c)  $\text{Al}_2\text{O}_3/\text{HfO}_2/\text{SiGe}$  bilayer, (d) and  $\text{Al}_2\text{O}_3\text{--HfO}_2$  Nanolaminate MOSCAPs. In these images, oxide structures and regions are defined according to  $z$  contrast. The interfacial layer between SiGe and oxide indicated with black and white arrows on corresponding STEM-HAADF, STEM-BF, and TEM image. Note in (b), the interlayer consists of both  $\text{SiGeO}_x$  and  $\text{Al}_2\text{O}_3$ , so it appears thicker than the control device in (a). In comparison to control device of  $\text{HfO}_2/\text{SiGe}$ , bilayer (c) and NL (d) show thinner interface consistent with remote  $\text{Al}_2\text{O}_3$  insertion reducing IL.

$\text{HfO}_2$  layers. Inset  $D_{it}$  values in Figure 4c,d denote the integrated defect density across the band gap and are in good agreement with the behavior observed for the peak  $D_{it}$ . As shown in Figures 2 and 4, the shapes of the  $D_{it}$  distributions for  $\text{HfO}_2/\text{SiGe}$  and  $\text{Al}_2\text{O}_3/\text{SiGe}$  are similar (not identical), but the  $D_{it}$  values vary more than 2 $\times$ ; this is consistent with the source of  $D_{it}$  being similar for both oxides (for example  $\text{GeO}_x$ ) but present in greater concentration for  $\text{HfO}_2/\text{SiGe}$  than  $\text{Al}_2\text{O}_3/\text{SiGe}$ .

In  $\text{Al}_2\text{O}_3$  ALD, during each TMA half cycle, the TMA is dosed in excess; therefore, after the surface hydroxyl groups are eliminated, the TMA is available to reduce additional species. However, during each  $\text{H}_2\text{O}$  half cycle, the  $\text{H}_2\text{O}$  is present in excess at the end of the pulse, and some  $\text{H}_2\text{O}$  or  $\text{H}_2\text{O}$ -derived species may diffuse through thin  $\text{Al}_2\text{O}_3$  gate stack. Also, although the  $\text{Al}_2\text{O}_3$  is a better diffusion barrier in comparison to the  $\text{HfO}_2$ , it has been reported previously that  $\text{GeO}_x$  can diffuse through thin  $\text{Al}_2\text{O}_3$  gate stacks.<sup>10</sup> The  $\text{Al}_2\text{O}_3\text{--SiGe}$  interface is known to include  $\text{GeO}_x$  species which are the source of interface defects.<sup>6</sup> It is hypothesized that above a critical thickness, the  $\text{Al}_2\text{O}_3$  becomes a good barrier to  $\text{H}_2\text{O}$ ; therefore, excess TMA exposure during ALD can scavenge oxygen from  $\text{GeO}_x$  species and convert it into Ge which might be redeposited on SiGe without the formation of new  $\text{GeO}_x$  from the water pulses.<sup>6</sup> This mechanism is consistent with decreasing  $D_{it}$  by insertion of  $\text{Al}_2\text{O}_3$  into  $\text{HfO}_2$ -containing gate dielectric stacks or deposition of  $\text{Al}_2\text{O}_3$  on top of  $\text{HfO}_2$  gate dielectrics. However, as noted earlier,  $\text{Al}_2\text{O}_3$  is a more effective diffusion barrier in comparison to  $\text{HfO}_2$  for oxygen containing species; consequently, the  $D_{it}$  suppression with  $\text{HfO}_2$  dielectrics is not expected to be as great as with  $\text{Al}_2\text{O}_3$

dielectrics of similar thickness.<sup>13</sup> This suggests that the number of  $\text{Al}_2\text{O}_3$  layers incorporated into oxide is mainly responsible for the interface defect density reduction observed in these experiments. Similar to  $6 \times (9\text{HfO}_2 + 1\text{Al}_2\text{O}_3)$  NL gate dielectric structure, gate oxide without an oxidant during  $\text{Al}_2\text{O}_3$  ALD is performed by only TMA dosing and  $D_{it}$  reduction along with  $C_{max}$  observed indicating  $\text{Al}_2\text{O}_3$  layer formation by oxygen scavenging. It is noted that for  $\text{HfO}_2$ -based gate stacks with incorporated  $\text{Al}_2\text{O}_3$  layers, the TMA may diffuse to the interface to directly reduce the  $\text{GeO}_x$  to Ge since  $\text{HfO}_2$  is a poor diffusion barrier; however, the mechanism likely co-exists with the remote scavenging mechanism.

Figure 5 shows STEM high-angle annular dark-field (HAADF), bright field (BF), and TEM images of the  $\text{HfO}_2$ -only,  $\text{HfO}_2\text{--Al}_2\text{O}_3$  bilayers, and nanolaminate gate stacks. White and black arrows in HAADF and BF images indicate the estimated oxide interfacial layer (IL) thickness. The SiGe– $\text{HfO}_2$  interface in Figure 5a shows a 0.8 nm IL. The insertion of  $\text{Al}_2\text{O}_3$  between SiGe and  $\text{HfO}_2$  increases the apparent IL thickness (Figure 5b) which is expected because the interface now consists of both  $\text{Al}_2\text{O}_3$  and  $\text{SiGeO}_x$ . EELS or another spatially resolved composition profiling method is needed to differentiate between these layers because of the similar atomic mass contrast of these oxides in HAADF-mode imaging.  $\text{Al}_2\text{O}_3$  grown on  $\text{HfO}_2$  and the  $\text{Al}_2\text{O}_3\text{--HfO}_2$  nanolaminate have a thickness similar that shown in Figure 5.

Elemental profiles across the gate stacks were investigated with STEM-EELS analysis, as shown in Figure 6. A multiple linear least square fitting procedure<sup>23</sup> is used to resolve spectroscopic feature overlay issues, especially for Al, Hf, and Si. The red dash line intercepts the half max of oxygen peak



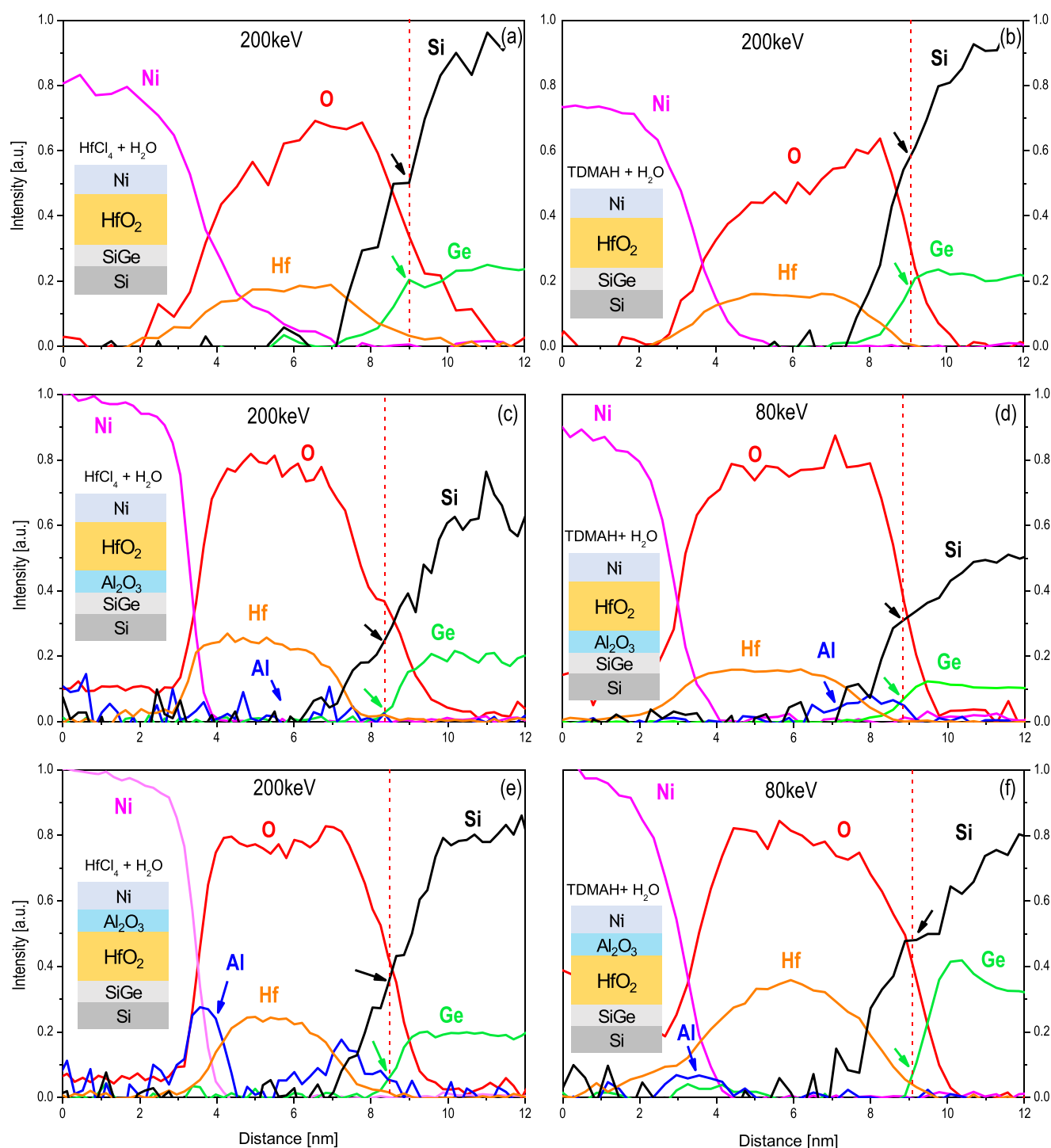


**Figure 6.** STEM-EELS compositional analysis of MOSCAP devices. EELS experiment performed at 80 and 200 keV as indicated. The inset drawings illustrate corresponding gate stack structure along with the ALD chemistry above it. The compositions of the elements are averages area of  $\sim 6 \times 0.2 \text{ nm}^2$  parallel to the sample surface. The red dashed line intercepts the half peak values of the O signals and indicates the SiGe–HfO<sub>2</sub> interface. Black and green arrows denote Si and Ge compositions on the SiGe surfaces, respectively. The blue arrow indicates the Al composition in the oxide. AlO<sub>x</sub>–HfO<sub>2</sub> interdiffusion is seen for bilayer samples regardless of the initial structure and confirmed with the raw data analysis in the figure and Figure S5. This interdiffusion is prominent for EELS analysis at 80 keV. In comparison to (a) and (b), devices in (c)–(f) show lower Ge/Si ratio at the intersection with red dashed lines indicate the Si rich interface formation with Al<sub>2</sub>O<sub>3</sub> incorporation into HfO<sub>2</sub>. Ni interdiffusion is seen in devices (a) and (b) and Al<sub>2</sub>O<sub>3</sub> insertion into HfO<sub>2</sub> impedes the Ni diffusion as seen in (c)–(f).

and is employed to indicate the SiGe surface. Black and green arrows denote Si and Ge compositions of the SiGe surface. It should be noted that the determination of interface location in STEM-EELS is subject to interpretation especially due to the surface roughness. However, even with the surface roughness,

the IL should be within few angstroms of the dashed lines, and this metric was confirmed by determining the location of the Si/SiGe interface since these layers are epitaxially grown. Any uncertainty in the exact location of the interface will not impact the trends in the elemental composition across the

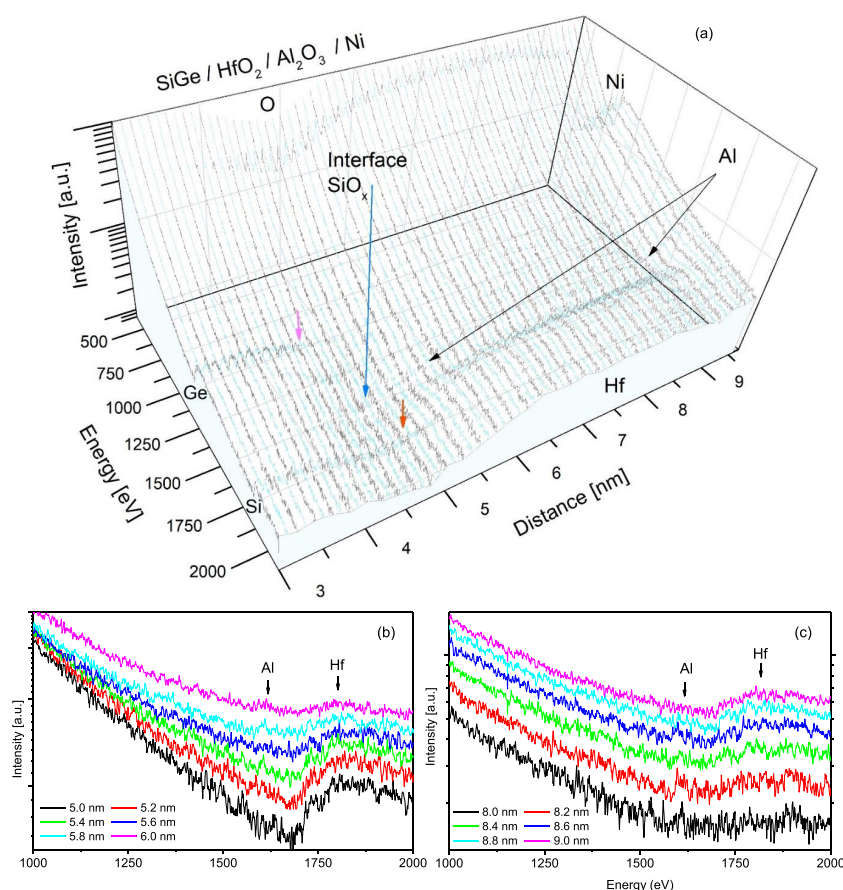


**Figure 7.** STEM-EELS compositional analysis of Ni/Al<sub>2</sub>O<sub>3</sub>/HfO<sub>2</sub>/SiGe MOSCAP device. Raw EELS data taken at 200 keV from the sample in Figure 6e is shown in a 3D semilog graph (a) with the energy axis indicating the electron energy loss and corresponding intensity in arbitrary units. The axis labeled with distance indicates the location of the electron beam on the sample. The colored consecutive black and light blue lines indicate electron energy loss for the given location on samples and two colors chosen to enhance the image contrast. Each data line projects energy loss averaged from areas of  $5 \times 0.2 \text{ nm}^2$  parallel to the sample surface. The peaks appear on the graphs corresponds to Si K edge (1839 eV), Ge L edge (1217 eV), Hf M edge (1662 eV), O K edge (532 eV), Al K edge (1560 eV), Ni L edge (885 eV). The blue arrow indicates the SiO<sub>x</sub> interface formation between SiGe and HfO<sub>2</sub>. Pink and red arrows indicate the Ge and Si compositions on SiGe surface. The Ge signal decays earlier than Si as it approaches the HfO<sub>2</sub> layer. Black arrows denote Al composition across the oxide. Al<sub>2</sub>O<sub>3</sub> insertion onto HfO<sub>2</sub> in bilayer structure forms intermixing by Al diffusion. To increase the visibility of Al peak and interdiffusion, semilog two-dimensional graph of raw EELS data with 1–2 K energy loss range is presented in graph (b) (SiGe/HfO<sub>2</sub> interface region) and (c) (HfO<sub>2</sub>/Ni interface region). Two graphs prepared with offsets introduced between each curve to improve the visibility.

oxide which indicates the suppression of Ge out-diffusion with Al<sub>2</sub>O<sub>3</sub> incorporation. Figure 6a,b shows 200 keV EELS analysis of the same structures fabricated with hafnium tetrachloride at 300 °C and tetradimethylamido hafnium(IV) ALD precursors at 275 °C; no significant differences were observed as seen in Figure 6a,b consistent with interface defects obtained with multifrequency C–V analysis. Both the HfCl<sub>4</sub> and TDMAH gate stacks have a nearly identical elemental distribution across the device and have a Ge tail extending about 2 nm into the HfO<sub>2</sub> layer in contrast to the capacitors in Figure 6c–f which show a diminished or zero Ge tail. This may be attributed to the Al<sub>2</sub>O<sub>3</sub> layer impeding Ge out-diffusion.<sup>11,13</sup> It is surprising that Al<sub>2</sub>O<sub>3</sub> reduces Ge out-diffusion even when Al<sub>2</sub>O<sub>3</sub> is deposited onto HfO<sub>2</sub> (Figure 6c–f). This may be the result of TMA reaction products (either AlO<sub>x</sub> or AlC<sub>x</sub>H<sub>y</sub>) diffusion into HfO<sub>2</sub> reaching IL.

Further documentation that even remote Al<sub>2</sub>O<sub>3</sub> ALD can control the GeO<sub>x</sub> in the interlayer is observed in the composition of the interlayers. For all of the gate stacks with Al<sub>2</sub>O<sub>3</sub>, the amount of Ge and the ratios of Si to Ge at the interface (between full max and 1/2 height of the oxygen peak)

are greater than the control HfO<sub>2</sub>/SiGe (Figure 6a); the exact comparison of the interfacial Si/Ge ratio between the samples with Al<sub>2</sub>O<sub>3</sub> (Figure 6b–f) is challenging since the ratio can vary with slight adjustment of the nominal interface position. All of the samples have an interlayer above the SiGe as shown by the gap between the Hf and O edges; however, the Si signal falls off most steeply for Si on the nanolaminate samples (Figures S5–S7) consistent with these samples having the most abrupt interface.

STEM-EELS at both 80 and 200 keV is employed to investigate the AlO<sub>x</sub> distribution in the ALD HfO<sub>2</sub> layer, while controlling beam induced Al damage due to high energy electrons.<sup>24</sup> For the HfO<sub>2</sub>/Al<sub>2</sub>O<sub>3</sub>/SiGe structures (Figure 6c,d), the 200 keV spectrum shows a complete diffusion of the Al, whereas the 80 keV spectrum shows only a small retention of Al at the interfaces likely due to the limited signal to noise of the 80 keV spectra; the data is consistent AlO<sub>x</sub> diffusing during the HfO<sub>2</sub> deposition. For the Al<sub>2</sub>O<sub>3</sub>/HfO<sub>2</sub>/SiGe structures (Figure 6e,f), the 200 keV spectrum shows two Al peaks, one above and one below HfO<sub>2</sub>, whereas the 80 keV spectrum shows a just small retention of AlO<sub>x</sub> above the HfO<sub>2</sub>



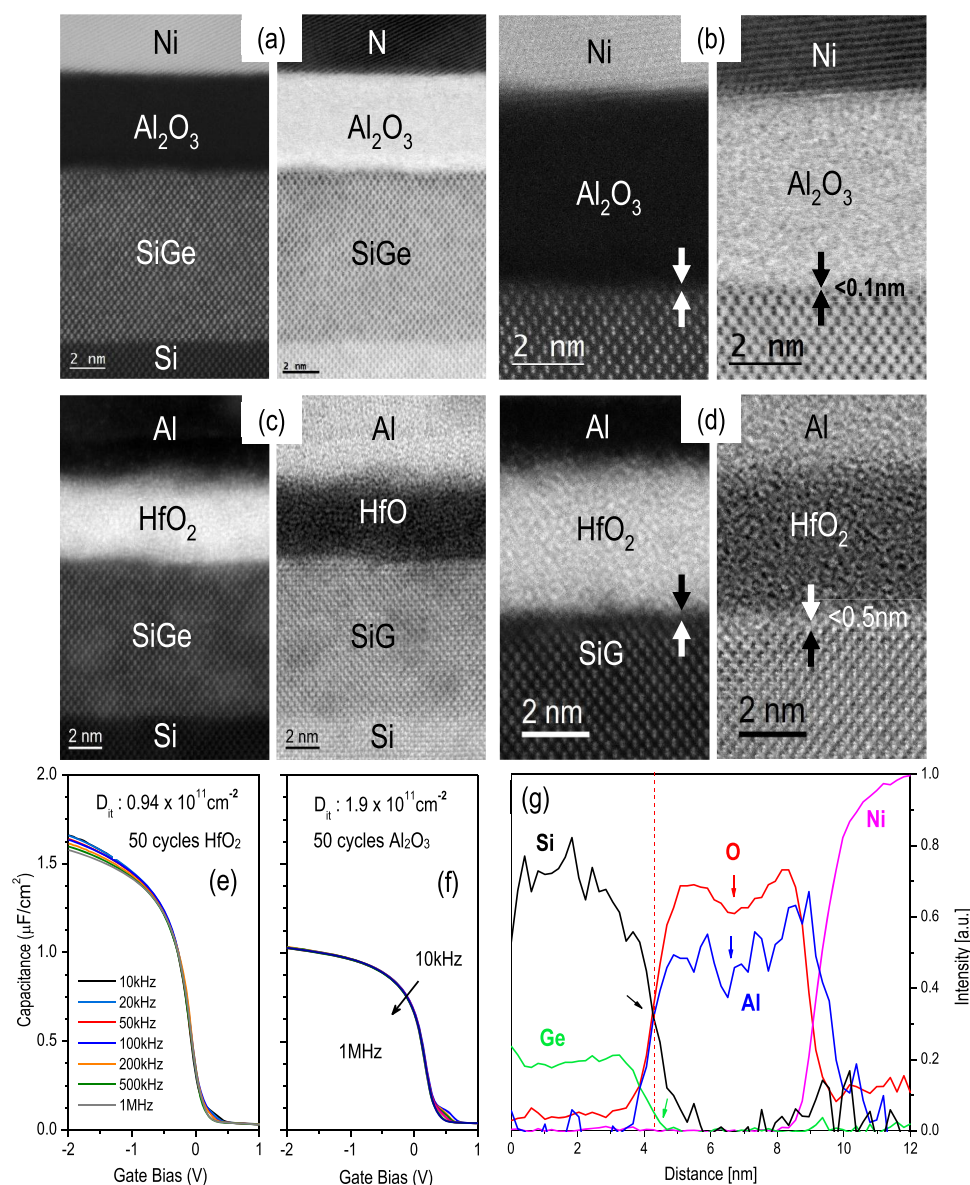


**Figure 8.** Comparison of Ni/Al<sub>2</sub>O<sub>3</sub>/SiGe/Si and Al/HfO<sub>2</sub>/SiGe/Si MOSCAPs. Note that the Al is a gettering gate metal. High-resolution STEM-HAADF and BF images at 80 keV of devices with (a, b) Ni/Al<sub>2</sub>O<sub>3</sub> and (c, d) Al/HfO<sub>2</sub> gate oxides; both have 50 ALD cycles. Nearly abrupt interfaces are observed in both bright field and dark-field imaging for both devices. (e, f) C–V graphs of Al/HfO<sub>2</sub> and Ni/Al<sub>2</sub>O<sub>3</sub> devices with very low depletion capacitance are shown, insets denote integrated  $D_{it}$  values across the band gap extracted with the full interface state model. EELS elemental composition of Ni/Al<sub>2</sub>O<sub>3</sub>/SiGe/Si is shown in (g). The regions of Al<sub>2</sub>O<sub>3</sub> gate oxide defined with z contrast in (a) and (b) are in good agreement with the EELS spectra in (g). The red dashed line intercepts the half peak values of the O, Si, and Ge signals and delineates the SiGe–HfO<sub>2</sub> interface. Black and green arrows denote Si and Ge composition on SiGe surface; a Si rich interface observed. The blue and red arrows indicate the electron beam damaged (80 keV) region of Al<sub>2</sub>O<sub>3</sub>. A similar effect also observed for samples studied at 2000 keV. Ni gate metal overlaying with Al indicating Ni and Al intermix. Note at the SiGe interface, the Al and O profiles are nearly identical consistent with a near zero SiGeO<sub>x</sub> interlayer.

layer, consistent with the limited signal to noise of the 80 keV spectra. Overall both are consistent with the diffusion of TMA or its reaction products into the HfO<sub>2</sub> when the Al<sub>2</sub>O<sub>3</sub> ALD is performed after HfO<sub>2</sub> ALD. The nanolaminate gate stack (Figure 1e) composition studied with 80 keV EELS shows dispersed Al (Figure S5).

This unexpected interdiffusion of Al<sub>2</sub>O<sub>3</sub> is also shown with EELS raw data in the three-dimensional (3D) semilog graph in Figures 7 (Ni/Al<sub>2</sub>O<sub>3</sub>/HfO<sub>2</sub>/SiGe) and S6 (Ni/HfO<sub>2</sub>/Al<sub>2</sub>O<sub>3</sub>/Ni). The oxide compositional profile can be seen from the electron energy loss peaks starting after element specific edges; for example, the Si K edge is at 1839 eV (orange arrow) and

the Ge L edges at 1217 eV (pink arrow). The blue arrow indicates the SiGe/HfO<sub>2</sub> interface region. It is seen that the Ge peak decays earlier than the Si peak as a function of distance from the SiGe surface consistent with a SiO<sub>x</sub> rich region at the interface. The black arrow indicates energy loss due to Al (K edge 1560 eV) across the oxide. The peak intensity is significantly lower in comparison to other elements; however, it can be seen in several regions in the HfO<sub>2</sub> and reaches a maximum close to the HfO<sub>2</sub>/Ni interface since it is deposited on HfO<sub>2</sub> as shown in 3D data and the region of interest in Figure 7a,b. However, the Al peak can be also seen close to SiGe/HfO<sub>2</sub> interface, almost 4 nm away where it was

deposited. The existence of Al signal in this region is consistent with  $\text{AlO}_x$  diffusion through  $\text{HfO}_2$ . A similar raw data analysis performed for  $\text{Ni}/\text{HfO}_2/\text{Al}_2\text{O}_3/\text{SiGe}$  bilayer device also shows interdiffusion (Figure S6). However, the comparison of EELS analysis for both bilayer structures indicates an enhanced  $\text{Al}_2\text{O}_3$ – $\text{HfO}_2$  interdiffusion when  $\text{Al}_2\text{O}_3$  is deposited prior to  $\text{HfO}_2$  ALD.

Figure 8 shows simultaneously acquired HAADF and BF-STEM images of  $\text{Ni}/\text{Al}_2\text{O}_3/\text{SiGe}/\text{Si}$  (a, b) and  $\text{Al}/\text{HfO}_2/\text{SiGe}/\text{Si}$  (c, d) MOSCAP devices along with corresponding  $C$ – $V$  graphs (e, f). In contrast to the  $\text{Ni}/\text{HfO}_2/\text{SiGe}/\text{Si}$  gate stack in Figure 5,  $\text{Al}/\text{HfO}_2/\text{SiGe}/\text{Si}$  has a gettering gate which is known to remove oxygen from the interfaces and reduces IL thickness; this is supported by EELS analysis (Figure S6) indicating similar O and Hf peak decay profiles at the SiGe interface unlike with Ni gates which show offsets between O and Hf peak at the interface (Figure 6a–f).<sup>16</sup>

The gate stacks in Figure 8e,f have two very dissimilar oxides and show very low depletion capacitance feature resulting from charging/discharging of interface traps. Similar integrated  $D_{it}$  values are displayed in the inset. However, these two very different gate oxide structures deposited on SiGe show similar, almost abrupt interfaces with the underlying SiGe (Figures S6 and 8g). For  $\text{Al}/\text{HfO}_2/\text{SiGe}$  capacitors, it was previously shown that an Al metal gate can scavenge oxygen from the interfacial layer and reduce the interface defect density while also thinning the IL.<sup>16</sup> For the case of the  $\text{Ni}/\text{Al}_2\text{O}_3/\text{SiGe}$  device, it is most likely that the introduction  $\text{Al}_2\text{O}_3$  ALD in the gate stack fabrication process provides an effect similar to that of an Al gate and scavenges oxygen from oxide/SiGe interface. The mechanisms are similar, because TMA is a highly reactive precursor with oxygen which can interact with nearly all oxygen containing molecules to form  $\text{Al}_2\text{O}_3$ . Insertion of each additional  $\text{Al}_2\text{O}_3$  layer using TMA precursor can scavenge excess oxygen from the gate oxide or the high- $k$ /SiGe interface. Similar to  $6 \times (9\text{HfO}_2 + 1\text{Al}_2\text{O}_3)$  NL gate dielectric structure, gate oxide without oxidant during  $\text{Al}_2\text{O}_3$  ALD is performed by only TMA dosing and  $D_{it}$  reduction along with  $C_{max}$  observed indicating  $\text{Al}_2\text{O}_3$  layer formation by oxygen scavenging. It is hypothesized that TMA exposure scavenges weakly bound oxygen from the interface either by diffusing into the interface as TMA or TMA reaction products (for example monomethyl aluminum) or it decomposes the  $\text{GeO}_x$  remotely, producing suboxide species that diffuse readily through even thin  $\text{Al}_2\text{O}_3$  (remote gettering).<sup>10</sup> As TMA interacts and scavenges oxygen from the interface, it is likely that  $\text{GeO}_x$  dissociates and donates oxygen to TMA due to the lower Gibbs free energy of formation of  $\text{GeO}_x$  in comparison to  $\text{SiO}_x$ .<sup>25</sup> Therefore, TMA can selectively scavenge oxygen from the interface layer and reduce the interface trap density, while also thinning the IL, which has important benefits for gate stack dimensional scaling.

STEM-EELS compositional analysis for the  $\text{Ni}/\text{Al}_2\text{O}_3/\text{SiGe}/\text{Si}$  device shown in Figure 8g supports this picture and indicates that a Si rich interface forms, as shown by the intersection of the red dashed line marking the SiGe surface and half maximum count-rate of oxygen. The black and green arrows denote the Si and Ge compositions at the oxide/SiGe interface, respectively. It is clearly seen that  $\text{GeO}_x$  composition is diminished significantly at the SiGe surface consistent with less diffusion of  $\text{GeO}_x$  into the gate oxide and less diffusion of  $\text{H}_2\text{O}$  through the  $\text{Al}_2\text{O}_3$  once the  $\text{Al}_2\text{O}_3$  reaches a critical thickness.

## CONCLUSIONS

Novel gate oxide structures were investigated which suppress electronic defects at high- $k$ /SiGe interfaces by employing an oxygen scavenging ALD precursor, TMA. The approach utilizes the difference in the heat of formation of  $\text{SiO}_x$  and  $\text{GeO}_x$ , achieving lower interface trap densities at the high- $k$ /SiGe interface with just a modest reduction of  $C_{max}$ . Although metallic Al remains more effective at oxygen scavenging, it induces a much larger  $C_{max}$  reduction, demonstrating the benefit of TMA remote oxygen scavenging. The data is consistent with the insertion of  $\text{Al}_2\text{O}_3$  into the  $\text{HfO}_2$  gate oxide, removing a  $\text{GeO}_x$  component of the interlayer between the channel and the deposited gate dielectric, and suggests that effective oxygen scavenging can be achieved with TMA during ALD. This TMA-based oxygen scavenging technique is most effective when the  $\text{Al}_2\text{O}_3$  layers are uniformly distributed across the  $\text{HfO}_2$  in a nanolaminate structure, but it also is effective when the  $\text{Al}_2\text{O}_3$  ALD deposition occurs on top of the  $\text{HfO}_2$ . To achieve the effect, during each TMA half cycle of  $\text{Al}_2\text{O}_3$  ALD, TMA is dosed in excess to provide sufficient TMA for the reduction of additional chemical species after the surface hydroxyl groups are eliminated. In the present study, for the first time, the mechanism for the low defect interface formation with  $\text{Al}_2\text{O}_3$  in contrast to  $\text{HfO}_2$  is explained with the experimental data. In contrast to previous reports, in which the good diffusion barrier properties of  $\text{Al}_2\text{O}_3$  are considered to be the source of  $D_{it}$  improvement, the mechanism for interface defect reduction with  $\text{Al}_2\text{O}_3$  in the present work is shown to be selective oxygen scavenging by diffusion of TMA reaction products in  $\text{HfO}_2$ . Furthermore, direct and remote oxygen scavenging using ALD  $\text{Al}_2\text{O}_3$  deposited on  $\text{HfO}_2$  gate oxide 4 nm away from SiGe surface is demonstrated. By deposition of  $\text{Al}_2\text{O}_3$  and etching back with atomic layer etching, it is likely that low  $D_{it}$  can be obtained in high aspect ratio structure such as on fins which is not possible with Al deposition for gettering gates.

## ASSOCIATED CONTENT

### Supporting Information

The Supporting Information is available free of charge on the ACS Publications website at DOI: 10.1021/acsami.8b22362.

Variation of interface defect density on samples as well as the comparison of interface defect calculation methods used in the article and the EELS analysis for few devices (PDF)

## AUTHOR INFORMATION

### Corresponding Author

\*E-mail: akummel@ucsd.edu.

### ORCID

Mahmut S. Kavrik: 0000-0002-0643-4964

Peter Ercius: 0000-0002-6762-9976

Kechao Tang: 0000-0003-4570-0142

Andrew C. Kummel: 0000-0001-8301-9855

### Notes

The authors declare no competing financial interest.

## ACKNOWLEDGMENTS

Larry Grissom, Sean Parks of the Nano3 clean room at UCSD are gratefully acknowledged for technical support. Work at the Molecular Foundry was supported by the Office of Science,

Office of Basic Energy Sciences, of the U.S. Department of Energy under Contract No. DE-AC02-05CH11231. Chung-Yang Lee, Yu-Chia Liang, and Vincent Hou from TSMC are appreciated for the discussions on EELS data analysis. This work was funded by TSMC and performed in part at the San Diego Nanotechnology Infrastructure (SDNI) of UCSD, a member of the National Nanotechnology Coordinated Infrastructure, which is supported by the National Science Foundation (Grant ECCS-1542148).

## REFERENCES

- (1) Fischetti, M. V.; Laux, S. E. Band Structure, Deformation Potentials, and Carrier Mobility in Strained Si, Ge, and SiGe Alloys. *J. Appl. Phys.* **1996**, *80*, 2234–2252.
- (2) Lu, D.; et al. (Invited) Silicon Germanium FinFET Device Physics, Process Integration and Modeling Considerations. *ECS Trans.* **2014**, *64*, 337–345.
- (3) Ceresoli, D.; Vanderbilt, D. Structural and Dielectric Properties of Amorphous h-k Oxides:  $\text{HfO}_2$ ,  $\text{ZrO}_2$  and Their Alloys. *Phys. Rev. B* **2006**, *74*, No. 125108.
- (4) ITRS 2.0. International Technology Roadmap for Semiconductors 2.0, 2015.
- (5) Taur, Y.; Ning, T. H. *Fundamentals of Modern VLSI Devices*; Cambridge University Press, 2013.
- (6) Zhang, L.; Guo, Y.; Hassan, V. V.; Tang, K.; Foad, M. A.; Woicik, J. C.; Pianetta, P.; Robertson, J.; McIntyre, P. C. Interface Engineering for Atomic Layer Deposited Alumina Gate Dielectric on SiGe Substrates. *ACS Appl. Mater. Interfaces* **2016**, *8*, 19110–19118.
- (7) LeGoues, F. K.; Rosenberg, R.; Nguyen, T.; Himpel, F.; Meyerson, B. S. Oxidation Studies of SiGe. *J. Appl. Phys.* **1989**, *65*, 1724–1728.
- (8) Cho, M.-H.; Chang, H. S.; Moon, D. W.; Kang, S. K.; Min, B. K.; Ko, D.-H.; Kim, H. S.; McIntyre, P. C.; Lee, J. H.; Ku, J. H.; Lee, N. I. Interfacial Characteristics of  $\text{HfO}_2$  Films Grown on Strained  $\text{Si}_{0.7}\text{Ge}_{0.3}$  by Atomic-Layer Deposition. *Appl. Phys. Lett.* **2004**, *84*, 1171–1173.
- (9) Chagarov, E.; et al. Density-Functional Theory Molecular Dynamics Simulations of a- $\text{HfO}_2$ /a- $\text{SiO}_2$ /SiGe and a- $\text{HfO}_2$ /a- $\text{SiO}_2$ /Ge with a- $\text{SiO}_2$  and a-SiO Suboxide Interfacial Layers. *Appl. Surf. Sci.* **2018**, *443*, 644–654.
- (10) Sardashti, K.; Hu, K.-T.; Tang, K.; Park, S.; Kim, H.; Madiseti, S.; McIntyre, P.; Oktyabrysky, S.; Siddiqui, S.; Sahu, B.; Yoshida, N.; Kachian, J.; Kummel, A. Sulfur Passivation for the Formation of Si-Terminated  $\text{Al}_2\text{O}_3$ /SiGe(001) Interfaces. *Appl. Surf. Sci.* **2016**, *366*, 455–463.
- (11) Lu, N.; Bai, W.; Ramirez, A.; Mouli, C.; Ritenour, A.; Lee, M. L.; Antoniadis, D.; Kwong, D. L. Ge Diffusion in Ge Metal Oxide Semiconductor with Chemical Vapor Deposition  $\text{HfO}_2$  Dielectric. *Appl. Phys. Lett.* **2005**, *87*, No. 051922.
- (12) Zhang, Q.; Wu, N.; Lai, D. M. Y.; Nikolai, Y.; Bera, L. K.; Zhu, C. Germanium Incorporation in  $\text{HfO}_2$  Dielectric on Germanium Substrate. *J. Electrochem. Soc.* **2006**, *153*, G207–G210.
- (13) Ogawa, S.; Asahara, R.; Minoura, Y.; Sako, H.; Kawasaki, N.; Yamada, I.; Miyamoto, T.; Hosoi, T.; Shimura, T.; Watanabe, H. Insights into Thermal Diffusion of Germanium and Oxygen Atoms in  $\text{HfO}_2$ /GeO<sub>2</sub>/Ge Gate Stacks and Their Suppressed Reaction with Atomically thin AlO<sub>x</sub> Interlayers. *J. Appl. Phys.* **2015**, *118*, No. 235704.
- (14) Kwak, I.; Kavrik, M.; Thomson, E.; Liang, Y.-C.; Ueda, S. T.; Tang, K.; Hou, V.; Lee, C.-Y.; Aoki, T.; Kim, M.; Fruhberger, B.; Taur, Y.; McIntyre, P. C.; Kummel, A. C.  $\text{HfO}_2$ /Al<sub>2</sub>O<sub>3</sub> Nanolaminate on  $\text{Si}_{0.7}\text{Ge}_{0.3}$ (100) Surface by Thermal Atomic Layer Deposition. ECS Meeting Abstracts MA2018-02, 2018; p 1080.
- (15) Chagarov, E. A.; Kavrik, M. S.; Fang, Z.; Tsai, W.; Kummel, A. C. Density-Functional Theory Molecular Dynamics Simulations of a- $\text{HfO}_2$ /a- $\text{SiO}_2$ /SiGe and a- $\text{HfO}_2$ /a- $\text{SiO}_2$ /Ge with a- $\text{SiO}_2$  and a-SiO Suboxide Interfacial Layers. *Appl. Surf. Sci.* **2018**, *443*, 644–654.
- (16) Kavrik, M. S.; Thomson, E.; Chagarov, E.; Tang, K.; Ueda, S. T.; Hou, V.; Aoki, T.; Kim, M.; Fruhberger, B.; Taur, Y.; McIntyre, P. C.; Kummel, A. C. Ultralow Defect Density at Sub-0.5 nm  $\text{HfO}_2$ /SiGe Interfaces via Selective Oxygen Scavenging. *ACS Appl. Mater. Interfaces* **2018**, *10*, 30794–30802.
- (17) Hua, W.; Lee, M. H.; Chen, P. S.; Maikap, S.; Liu, C. W.; Chen, K. M. Ge Outdiffusion Effect on Flicker Noise in Strained-Si nMOSFETs. *IEEE Electron Device Lett.* **2004**, *25*, 693–695.
- (18) Hinkle, C. L.; Sonnet, A. M.; Vogel, E. M.; McDonnell, S.; Hughes, G. J.; Milojevic, M.; Lee, B.; Aguirre-Tostado, F. S.; Choi, K. J.; Kim, H. C.; Kim, J.; Wallace, R. M. GaAs Interfacial Self-Cleaning by Atomic Layer Deposition. *Appl. Phys. Lett.* **2008**, *92*, No. 071901.
- (19) Milojevic, M.; Contreras-Guerrero, R.; Lopez-Lopez, M.; Kim, J.; Wallace, R. M. Characterization of the “Clean-up” of the Oxidized Ge(100) Surface by Atomic Layer Deposition. *Appl. Phys. Lett.* **2009**, *95*, No. 212902.
- (20) Chen, H. P.; Yuan, Y.; Yu, B.; Ahn, J.; McIntyre, P. C.; Asbeck, P. M.; Rodwell, M. J. W.; Taur, Y. Interface-State Modeling of Al<sub>2</sub>O<sub>3</sub> InGaAs MOS From Depletion to Inversion. *IEEE Trans. Electron Devices* **2012**, *59*, 2383–2389.
- (21) Chen, H.-P.; Yuan, Y.; Yu, B.; Chang, C.-S.; Wann, C.; Taur, Y. Re-examination of the Extraction of MOS Interface-State Density by C–V Stretchout and Conductance Methods. *Semicond. Sci. Technol.* **2013**, *28*, No. 085008.
- (22) Nicollian, E. H.; Brews, J. R. *MOS (Metal Oxide Semiconductor) Physics and Technology*; Wiley-Interscience: New York, 1982.
- (23) Leapman, R. D.; Swyt, C. R. Separation of Overlapping Core Edges in Electron Energy Loss Spectra by Multiple-Least-Squares Fitting. *Ultramicroscopy* **1988**, *26*, 393–403.
- (24) Jiang, N. Electron Beam Damage in Oxides: a Review. *Rep. Prog. Phys.* **2016**, *79*, No. 016501.
- (25) Reed, T. B. *Free Energy of Formation of Binary Compounds: An Atlas of Charts for High-Temperature Chemical Calculations*; MIT Press, 1971.